Probing electronic structure of stoichiometric and defective SnO₂

M. S. Moreno,[1] J. J. Kas,[2] C. Ma,[3] F. Wang,[4,*] J. J. Rehr,[2] and M. Malac[4]

[1]*Centro Atómico Bariloche, 8400-San Carlos de Bariloche, Argentina*
[2]*Department of Physics, University of Washington, Seattle, Washington 98195, USA*
[3]*Center for High Resolution Electron Microscopy, College of Materials Science and Engineering, Hunan University, Changsha 410082, People's Republic of China*
[4]*National Institute for Nanotechnology, 11421 Saskatchewan Drive, Edmonton, Alberta T6G 2M9, Canada*

The electronic structure of stoichiometric tin dioxide (SnO₂) is studied by probing its unoccupied states using the fine structure in the electron energy-loss spectra (EELS) at the oxygen-K (O-K) edge. The spectral measurements were performed both at room and at high temperatures (773 K) and compared to *ab initio* calculations carried out using the real-space multiple-scattering and linearized augmented-plane-wave methods. Important many-body effects are included via quasiparticle corrections calculated within the many-pole GW self-energy approximation. An additional energy-dependent damping is calculated to account for vibrational effects. Results from this paper demonstrated that quantitative agreement between theoretical and experimental spectra can be obtained when nonspherical potentials and quasiparticle self-energy effects are considered and vibrational broadening is included. Modifications of the electronic structure by single oxygen vacancies, both in the bulk and at the (110) surface, also are predicted. Our predictions support the use of O-K EELS as a probe of the defect structures in SnO₂ surfaces and nanoparticles.

I. INTRODUCTION

Tin dioxide (SnO₂) is a prominent *n*-type semiconductor with widespread technological applications, *such as* gas sensing [1–5], catalysis [6,7], field effect transistors [8,9], organic solar cells [10,11], lithium ion batteries [12–14], and supercapacitors [15,16]. Knowledge of its electronic properties is key to understanding and predicting the efficacy of the materials used in these applications. In addition, it is well known that the response of materials to gas sensing strongly depends on its operating temperature [17] since it affects the electron mobility and electrical conductivity, which in turn depend on the crystal structure and stoichiometry-dependent surface states [18,19]. It has been determined that the SnO₂-based sensors for different gases generally are operated at temperatures below 720 K [20,21].

Current efforts are under way to obtain different nanostructured forms and engineered facets of SnO₂ as a way to manipulate and control its band structure and related electronic properties [15,22]. Most of the observed properties are sensitive to bulk or surface stoichiometry since they involve removal of electrons from the conduction band with oxygen vacancies being responsible for some of the observed effects or its enhancement [1,2,23–26].

Undoped SnO₂ is a transparent wide-band-gap semiconductor; however its electronic conductivity may be induced by native defects. High-temperature gravimetric studies indicate a very narrow degree of oxygen nonstoichiometry in tin dioxide, namely, SnO$_{2-x}$ with $x = 2 \times 10^{-4}$ at 1423 K [27]. The *n*-type behavior is attributed to these intrinsic oxygen vacancies [28,29]. A recent computational study has shown that a single oxygen vacancy is the defect with the lowest formation energy

[30], compared to other more complex defect configurations, such as clusters of oxygen vacancies and interstitial tin. The effect of the oxygen vacancies on the electronic structure is the introduction of shallow levels close to the minimum of the conduction band and deeper intragap energy levels [31], which have been assumed to be responsible for the luminescence and gas sensing properties of SnO₂ nanocrystals [23–26]. Although high-angle annular dark-field (HAADF) imaging in scanning transmission electron microscopy (STEM) allows the detection of single impurity atoms with an appropriate atomic number (Z) difference with the support, imaging of the impurities or vacancies of low-Z elements, such as oxygen, is substantially more challenging.

The goal for understanding the mechanisms and properties that lead to enhanced performance in the above applications has stimulated the study of occupied and near gap states. Comparison of experiment and theory mainly covers the occupied states or the near gap states [32]. However, the unoccupied states are also of fundamental interest since they play a major role in determining material properties when defects or adsorbates are present at finite temperatures. So far, high quality experimental data related to the unoccupied states of SnO₂ have been limited to a few soft x-ray absorption (XAS) measurements at the O-K edge [33,34] or EELS of both Sn-$M_{4,5}$ and O-K edges [35,36]. Both XAS and EELS involve electronic transitions between an initial (occupied) core state and a final (unoccupied) state. In addition, these techniques are dominated by dipole transitions. In consequence, the information content of EELS is similar to that of x-ray absorption near-edge spectra (XANES), and the fine structure present in the spectrum reflects a (local) angular momentum-projected unoccupied density of states [37].

To our knowledge there has been only one study combining experimental and theoretical EELS spectra of the O-K edge [36] of SnO₂, wherein the observed spectrum of the O-K edge could not be reproduced adequately using the current theory.

---

*Present address: Sustainable Energy Technologies Department, Brookhaven National Laboratory, Upton, New York, 11973, USA.

In this paper, we show an adequate theoretical reproduction of this edge for stoichiometric SnO_2.

Here, we use theoretical calculations to investigate the effects of O vacancies on the EELS and electronic structure of SnO_2, together with comparisons with high quality experimental EELS data of stoichiometric SnO_2 to validate our theoretical approximations. Although different theoretical works have shown changes in the density of states with defects [29,30], we report on their impact on the EELS spectrum. Here we search for possible distinctive signatures in the O-K-edge EELS due to the presence of oxygen vacancies. We have calculated the EELS fine structure at the O-K edge using the real-space multiple scattering (using the FEFF code) as well as the linearized augmented-plane-wave (LAPW) methods (using WIEN2K) which incorporates the effects of nonspherical potentials. For both approaches we go beyond conventional density-functional-theory- (DFT-) based methods by including quasiparticle corrections and lifetimes as well as vibrational broadening to give a quantitative account of inelastic losses [38,39].

The remainder of this paper is organized as follows. Section II describes the experimental EELS measurements. Section III gives details of the calculations, including those of WIEN2K and FEFF, as well as the application of the many-pole self-energy and vibrational broadening models. Results are presented and discussed in Sec. IV, and concluding remarks are given in Sec. V.

II. EXPERIMENTAL METHODS

Commercial powder of SnO_2 (Sigma-Aldrich, 99.995 + % purity) was dispersed onto a continuous carbon film supported on a Mo grid. The samples have particles with minimum sizes of about 40 nm. We measured EELS spectra both at room temperature and at 773 K in a JEOL 2200FS microscope equipped with an in-column Ω filter. A Gatan 652 double-tilt heating holder was used. During heating a slight change in the vacuum level was observed between 373 and 473 K, suggesting desorption of gases from the sample holder, the microscope hardware, and the sample itself (both from the crystal surface and/or from the carbon support). The energy resolution, estimated from the full width at half maximum of the zero loss peak, was 0.9 eV. Energy-loss spectra were measured from many nanoparticles in the diffraction mode with a collection semiangle of 6 mrad. The diameter of the area illuminated by the beam was about 20 nm. Our spectra were obtained from nanoparticles of sizes below 60 nm and from different thin areas with relative thicknesses of about 0.25.

III. CALCULATIONS

A. WIEN2K

Electronic structure calculations were performed using the full potential LAPW method within DFT via the WIEN2K code [40], and the energy-loss near-edge structure (ELNES) spectra were simulated using the TELNES3 program [41]. In the calculations we used the experimental crystal structure parameters [42]. The exchange-correlation potential was treated by the generalized gradient approximation of Perdew-

Burke-Ernzerhof [43]. The muffin-tin radii R_{mt} were 2.1 and 1.7 a.u. for Sn and O atoms, respectively. The maximum angular momentum of the radial wave functions was set to 10, and $R_{mt} K_{max}$ was fixed at 7.0 to set the basis size. The energy cutoff to separate core from valence states is -6.0 Ry. For the oxygen-K spectra we included core-hole effects using a supercell and found convergence with a $2 \times 2 \times 3$ cell, similar to previous findings [44]. We used 1056 irreducible Brillouin-zone k points for the primitive cell and 36 irreducible k points for the $2 \times 2 \times 3$ supercell when calculating the ELNES spectra. During the self-consistent-field (SCF) cycle calculation, the charge and energy convergence were set to 0.000 01 e and 0.0001 Ry, respectively. The core-hole effect on the O-K edges was treated in such a way that one electron was removed from the core level (1s state) of one oxygen atom and then the extra electron was taken as the background charge to the supercell in order to preserve the electric neutrality.

B. FEFF

The O-K edge was calculated for stoichiometric SnO_2 using the FEFF9 code [45], which is based on an *ab initio* self-consistent real-space multiple-scattering approach [46]. Accurate and well-converged spherical muffin-tin potentials, electron densities, and the Fermi level are calculated in a SCF procedure [47]. The EELS module in FEFF9.6 allowed us to take into account experimental parameters, such as beam energy, convergence, and collection semiangles as well as sample-to-beam orientation [45]. Convergence of the calculations was evaluated by changing the size of the cluster used [48]. We found that a cluster of about 60 atoms was sufficient to obtain well-converged SCF potentials. For the full multiple-scattering calculations a cluster size of 226 atoms was used. The FEFF calculations were performed with the Hedin-Lundqvist self-energy (i.e., complex energy-dependent exchange-correlation potentials) to account for inelastic losses. In the construction of the muffin-tin potentials, we allowed for different degrees of overlapping of the muffin tins in order to reduce discontinuity effects at the edges of the muffin tins and to roughly estimate the need for nonspherical corrections to the potentials [36]. Core-hole screening effects were included using the random-phase approximation. In order to evaluate the changes introduced by the oxygen vacancies we used different potentials for the oxygen and tin atoms closest to the vacancy.

C. Quasiparticle self-energy and vibrational effects

Many-body electronic self-energy and vibrational effects cause shifts in the position as well as broadening of peaks in excited-state electronic spectra, such as EELS or XAS relative to those calculated using static mean-field theories, such as density functional theory. In this paper we included the quasiparticle effects through the GW many-pole self-energy model [38] (GW is the Hedin self-energy model, where G is the Green's function and W is the screened Coulomb interaction), whereas vibrational broadening was approximated using an additional imaginary self-energy matched to the Debye-Waller factors found in extended x-ray absorption fine-structure (EXAFS) analysis [39].

The many-pole model is based on a generalization of the Hedin-Lundquist GW plasmon-pole self-energy commonly used in calculations of XAS and replaces the single plasmon pole with a sum of weighted poles to represent the true loss function of the material, i.e.,

$$\text{Im}[\epsilon(q,\omega)^{-1}] = \pi \sum_i g_i \omega_i^2 \delta[\omega^2 - \omega_i(q)^2].$$

Within this approximation, the self-energy is given by a static exchange part plus a sum of the single-pole correlation self-energies,

$$\Sigma(k,E) = \Sigma_{ex}(k) + \sum_i g_i \Sigma_c(k,E;\omega_i).$$

The weights ω_i and positions g_i of the poles are matched to the zero momentum transfer loss function, which can be approximated within the FEFF code or provided as input taken from experimental results or higher quality calculations, such as those based on the Bethe-Salpeter equation (AI2NBSE, EXCITING, YAMBO). Several sum rules are useful for correcting calculated and experimental loss functions. Of particular importance are the first moment or f-sum rule and the first inverse moment, which is related to the high-frequency dielectric constant of the material, i.e.,

$$\frac{1}{\epsilon_\infty} = 1 + \frac{2}{\pi} \int d\omega' \frac{\omega' \text{Im}[\epsilon(\omega')^{-1}]}{\omega' - \omega},$$

where ϵ_∞ is the electronic contribution to the static dielectric constant. Whereas the rough approximations made in the FEFF-calculated loss function tend to preserve the f-sum rule, the inverse moment is more difficult to reproduce *ab initio*. Thus the user has the option to provide the dielectric constant as input, and the sum rule is enforced by scaling the positions and amplitudes of the poles to match the inverse moment while preserving the first moment. In our many-pole calculations, we took the dielectric constant to be 4.95 [49].

Vibrational effects are approximated via an additional purely imaginary self-energy correction,

$$\Sigma_{\text{DW}}(E) = -\frac{ik^3\sigma_0^2}{R_0},$$

where $R_0 = 2.052$ Å is the nearest-neighbor (NN) bond length, $\sigma_0^2 = 0.0035$ Å^2 [50] is the mean-square relative displacement of the nearest-neighbor bond, and $k = \sqrt{2(E-E_0)}$ is the EXAFS wave number as measured from the edge energy E_0. This approximation provides a reasonable estimate of the energy-dependent broadening due to static and vibrational disorder (as also seen in the extended x-ray absorption fine structure). However, this approximation does not affect the low-energy XANES peaks and does not include symmetry breaking, which can cause transitions to dipole forbidden peaks. Although this might be problematic for some systems, there is no indication that this occurs at the O-K edge in SnO$_2$.

Finally, the total self-energy can be used within the definition of the Green's function in FEFF or applied to the spectrum via a postprocessing convolution with an energy-dependent spectral function as was performed for the WIEN2K results [51].
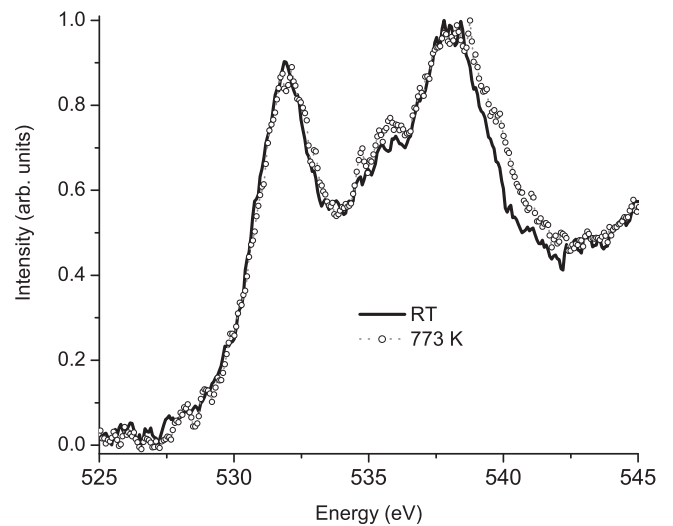

FIG. 1. EELS spectra of the O-K edge from a SnO$_2$ sample, obtained at room temperature (solid line) and at 773 K (dashed-circle line).

IV. RESULTS AND DISCUSSION

A. Stoichiometric SnO$_2$

The spectra obtained at room temperature and at 773 K are shown in Fig. 1. The similarity between both spectra is clear. Our spectra for SnO$_2$ are in full agreement with that previously reported for the oxygen edge by EELS [36], x-ray absorption spectroscopy at room temperature, and ambient atmosphere [33,34]. The fine structure within the first 10 eV above threshold has two main peaks separated by about 6.6 eV with a third peak appearing at about 536.2 eV and a minor one observed as a shoulder at 539.4 eV. The same fine structure was observed in aerogels with smaller particle sizes of about 3–5 nm [35]. In consequence we conclude that the observed fine structure corresponds to the intrinsic bulk electronic properties of this material, which still needs to be reproduced theoretically.

Figure 2 shows a comparison of the FEFF-calculated spectra using the single-pole (solid black) sum-rule-corrected many-pole approximations for the self-energy, including the knowledge of the dielectric constant (EPS0), using the calculated loss function (light gray) and the experimental loss function (black dot-dashed line) along with the experimental data (open circles). Clearly the use of the many-pole model along with vibrational broadening improves the calculated spectrum as compared to experiment, providing a roughly 14% stretch in the peak positions relative to the single-pole calculation. The importance of the energy-dependent broadening coming from the combined electronic and vibrational effects is not clearly apparent in this comparison but will be seen later when comparing the WIEN2K calculations. The use of the experimental loss function improves the agreement with experiment. This result emphasizes the utility of acquiring the low-energy loss function during EELS experiments, which is relatively easy to do. Note that the present combination of theory and experimental information is not restricted to the material under study but is general.
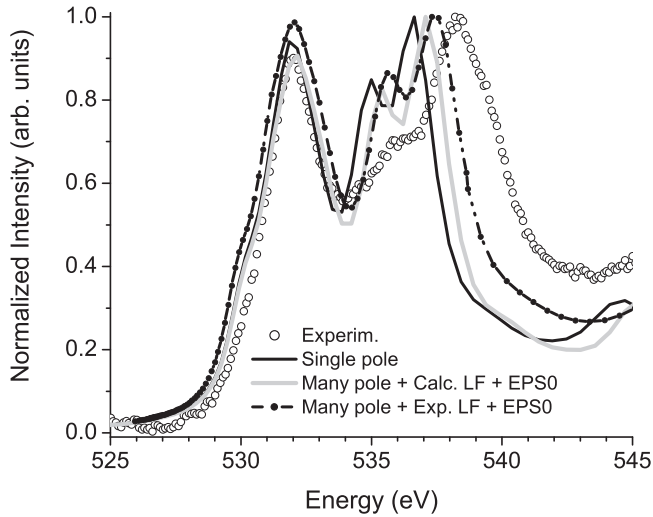
FIG. 2. Oxygen-K-edge spectra from SnO_2. Experimental: open circles; calculated using FEFF: single pole (black solid line), many poles with a calculated loss function and EPS0 (light gray), and many poles with an experimental loss function and EPS0 (black dashed-dot line).

Figure 3 shows the spectra obtained using WIEN2K for supercells of two different sizes and compared to experiment. There are noticeable changes in the spectrum when the bigger $2 \times 2 \times 3$ supercell is used. An increase in the supercell size to $3 \times 3 \times 3$ does not show significant changes as observed in the figure, consistent with previous findings [44]. The requirement of a $2 \times 2 \times 3$ supercell can be understood in terms of the unit-cell parameters of SnO_2 with lattice parameters of $a = 4.737$ and $c = 3.186$ Å. The size of the $2 \times 2 \times 3$ supercell is very approximately the same and about 9.5 Å. This distance seems to be sufficient to prevent any noticeable effects of core-hole periodicity on the spectrum. We can observe a richer fine structure when using the $2 \times 2 \times 3$ cell, showing all the peaks
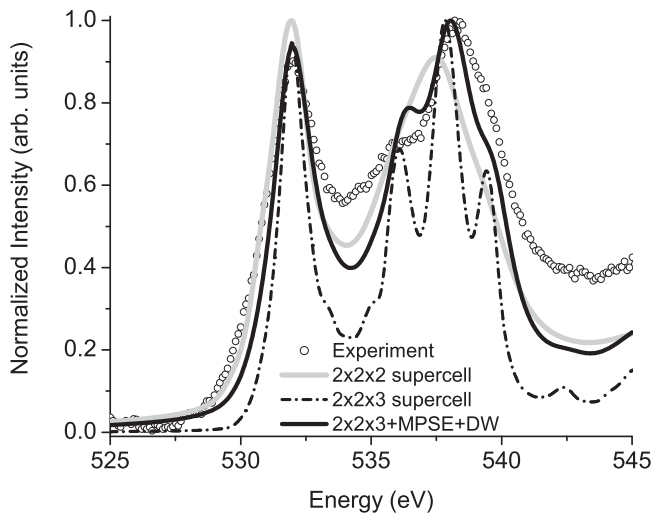

FIG. 3. Oxygen-K-edge spectra from SnO_2. Experimental: open circles; calculated using WIEN2K for supercells of different sizes. The black solid line corresponds to a $2 \times 2 \times 3$ spectrum convolved to account for the self-energy.
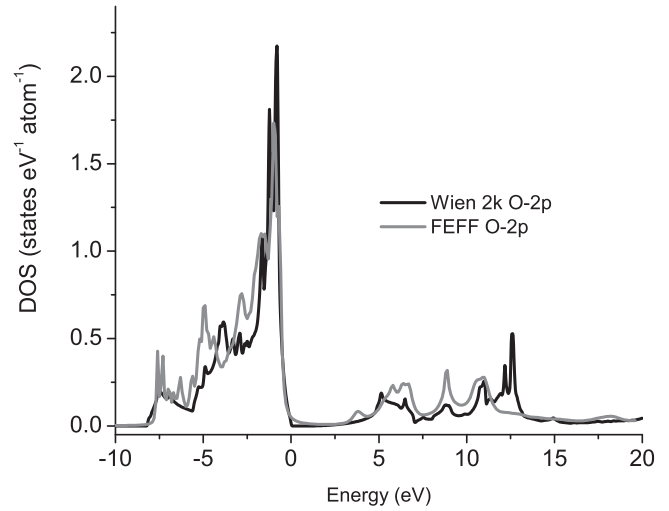

FIG. 4. Oxygen p DOS obtained from calculations using FEFF (gray line) and WIEN2K (black line). The zero of energy is the Fermi level.

present in the experiment. The black solid line corresponds to the spectrum of the $2 \times 2 \times 3$ supercell convolved to account for the self-energy as described in Sec. III C.

Because FEFF and WIEN2K use different potentials, it is not *a priori* clear whether the differences in spectra obtained are due to full potential effects or differences in the core-hole potential. In order to check the muffin-tin approximation in Fig. 4 we compare the local density of states (DOS) obtained without a core hole from both WIEN2K and FEFF. Both DOS have a similar structure except for the peak at about 12.5 eV above Fermi level, which is not present in FEFF DOS. This finding points to the spherical muffin-tin potential approximation used in FEFF as being responsible for the lack of minor details in the fine structure, such as the shoulder at about 539.4 eV.

B. Oxygen-deficient SnO_2

Although FEFF does not clearly reproduce the fine and minor details present in the O-K spectrum, we consider it important to realize that FEFF reproduces the main fine structure consisting of three peaks, which is useful as an experimental fingerprint of this compound, particularly in the phase identification of nanostructured materials. In other words, if important changes appear in the fine structure FEFF could be used for these studies, allowing us to still take advantage of the efficiency and flexibility of the real-space multiple-scattering method, yielding fast *ab initio* EELS results for clusters of arbitrary shapes and stoichiometries.

Due to the tetragonal symmetry of SnO_2, there are four O-O distances within the coordination octahedra of tin, i.e., each oxygen has four different oxygen NNs at distances of 2.586 Å (A-O_1 atoms), 3.186 Å (along the z axis), 4.103 Å (diagonal) on the octahedral basal plane, and at 2.905 Å, the distance between the oxygen atoms on the basal plane and the apical oxygen (see Fig. 5). Single oxygen vacancies should be compensated by reduction of the Sn atoms NNs to the vacancy to the Sn^{2+} state.
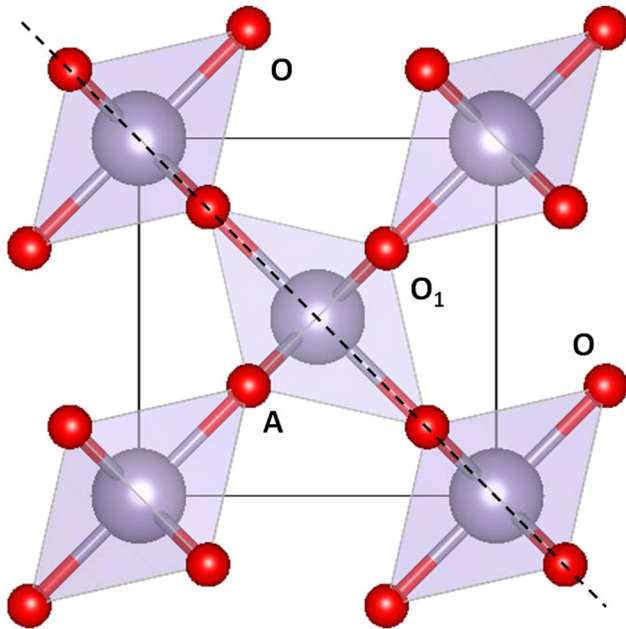
FIG. 5. A schematic polyhedral representation of the tetragonal structure of SnO_2 along the c axis. The red circles represent oxygen atoms, and the bigger circles in the center of the octahedron represent tin atoms. The black dashed line indicates the (110) plane.

In the description of defective SnO_2 we use different potentials for atoms near neighbors to the vacancy and more distant atoms. The charge transfer is obtained self-consistently during the SCF procedure by subtracting the total charge counts (obtained from the occupation numbers in the self-consistent calculations) from the neutral pure atomic configurations. Table I shows the charge transfer for stoichiometric and defective SnO_2 containing a single oxygen vacancy. The ratio of the charge transfers is proportional to the formal valence numbers of Sn and O in the stoichiometric compound and for the atoms located outside the first coordination shell of O and Sn (i.e., not nearest neighbors). This ratio approaches to one for the oxygen vacancy at a second or third NN position, indicating tin is reduced to the 2+ oxidation state as expected.

The calculated DOS for the stoichiometric and oxygen-deficient materials present similar structures and a few differences. For comparison we shift and align the valence DOS of the stoichiometric structure to the DOS of the oxygen-deficient one. The main differences are visible in the near band-gap region as can be appreciated in Fig. 6 (upper panel).

TABLE I. Charge transfer for stoichiometric and defective tin dioxide. Sn NN and O NN are tin and oxygen atoms neighboring the oxygen vacancy.

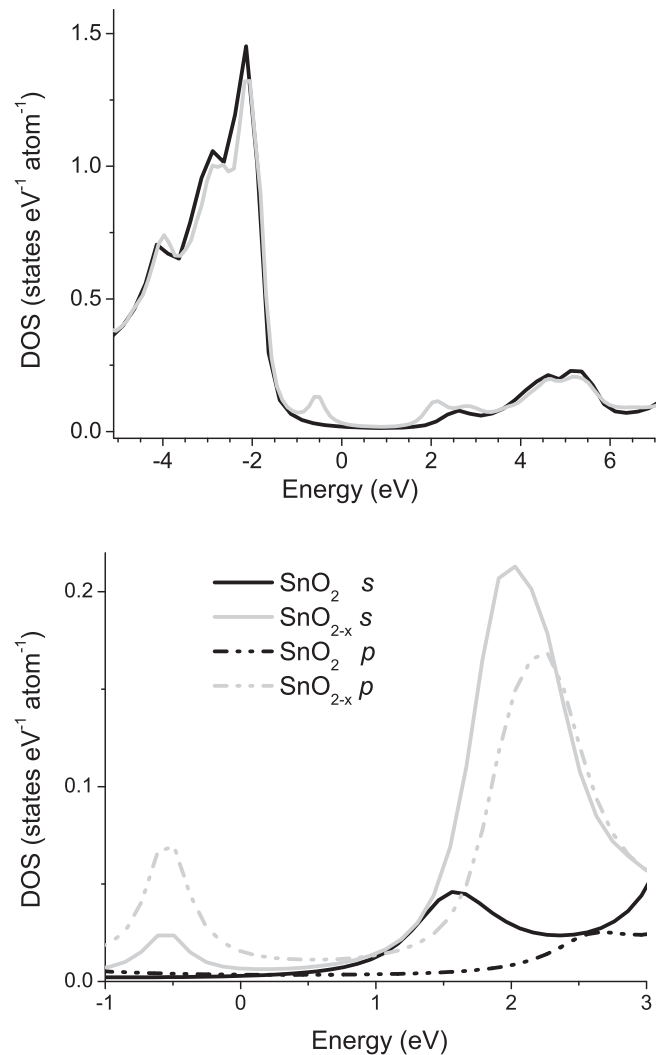|	Charge
Sn	-0.663
O	0.331
Sn-NN vac	-0.383
O-NN vac	0.348

FIG. 6. (Upper panel) Oxygen p DOS of stoichiometric SnO_2 (black line) and with a 1st NN oxygen vacancy (gray line). (Bottom panel) Details of the Sn s DOS (solid lines) and p DOS (dashed lines). The zero of energy is the Fermi level of oxygen-deficient SnO_2.

The comparison clearly shows that the oxygen vacancy introduces occupied states at about 1 eV above the top of the valence band and empty states below the minimum of the conduction band of the stoichiometric material, reducing the band gap. The conduction band is shifted to higher energies by about 0.4 eV. Thus the vacancy is responsible for both the blueshift of the conduction-band states and the appearance of a strong peak at about 1 eV above Fermi level. The trend observed here is in agreement with previous calculations [31] and experimental literature that place donor levels for oxygen vacancies up to 0.3 eV below the conduction band upon reducing a stoichiometric surface [25,26,52]; these donor levels would be responsible for the low-temperature gas sensing properties. Theoretical work usually report total density of states or partial density of states without details of variations for each component in this energy region. Our results shown in the bottom panel of Fig. 6 indicate that the unoccupied Sn p states move to lower energies by 0.4 eV and
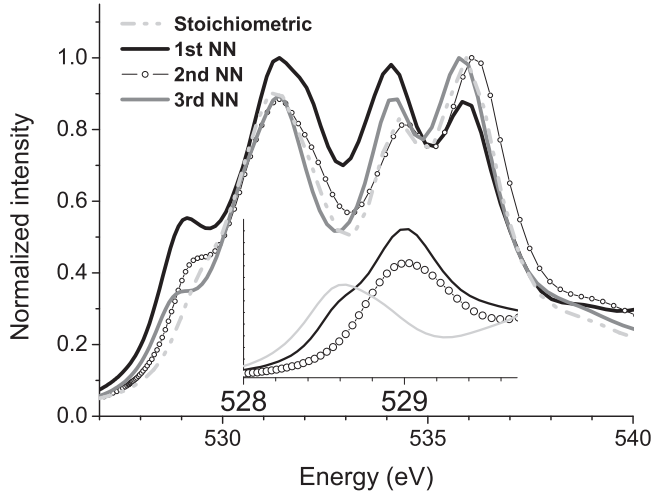
FIG. 7. Oxygen-K-edge spectra from SnO_2 with a single oxygen vacancy located at different positions as labeled in the legend. The spectrum for stoichiometric compound is included. The inset shows the energy region of the prepeak and its subtle variation in the energy position.

FIG. 8. Oxygen p DOS of stoichiometric bulk SnO_2 (black line), stoichiometric (110) surface (gray dashed- dot line), and (110) surface with an oxygen vacancy (gray line).

that the oxygen states lying at about 3 eV above Fermi level are split in the presence of the oxygen vacancy.

All the structures in the DOS appearing within the first 10 eV above Fermi level arise from a covalent mixing of O $2p$ and Sn $5s$-p. In particular, in stoichiometric SnO_2 the Sn contribution to the peak at about 3 eV in SnO_2 is mainly due to the s states [36]. In the reduced material the shift of the Sn $5p$ states to lower energy makes the peak at about 2 eV more equally contributed by Sn s and p states, also resulting this peak in hybridized O $2p$-Sn $5s$-p states.

We explore the effect of the changes in the electronic structure reflected by the fine structure of the electron energy-loss spectrum due to the presence of oxygen vacancies for the different locations of the vacancy. In Fig. 7, the calculated spectra are shown for an incident electron beam along the (001) orientation with a collection angle of 10 mrad for a vacancy located as the first nearest neighbor (1st NN), second NN (2nd NN), and third NN. The corresponding spectrum for stoichiometric SnO_2 is included for comparison. In all cases we see a distinctive additional peak at about 529 eV with a subtle but distinguishable variation in the energy position as shown in the inset of Fig. 7. The presence of this prepeak is the main change in the spectrum. The intensity of this peak is higher for the 1st NN vacancy and decreases with the distance of the vacancy to the absorber. Another effect is the modification of the peak intensity ratio, being stronger for the 1st NN vacancy. Note that the spectra contain the experimental broadening present in our experiment. In the inset this broadening is not included, suggesting that the detection of this prepeak would benefit by the use of a monochromator.

Some experimental reports or predictions of such changes in the spectrum are shown in this paper. Because the concentration of oxygen vacancies in SnO_2 is intrinsically very low, we suggest that the detection of such changes should be favored by using STEM-HAADF in an aberration-corrected electron microscope.
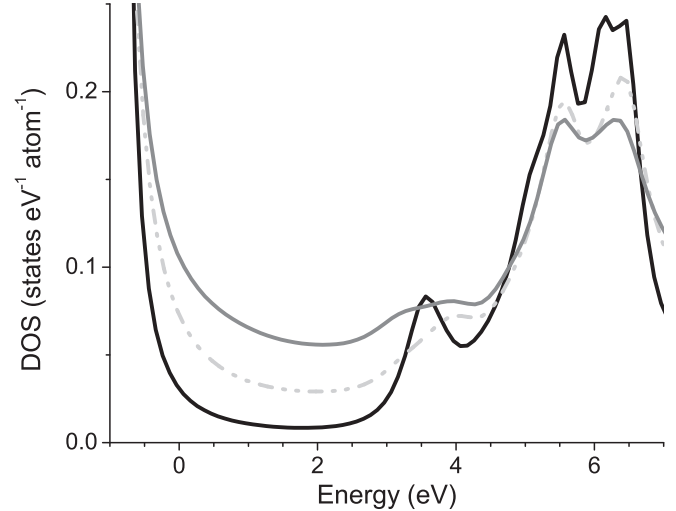
Low-temperature sensing response has been correlated to oxygen vacancies on the surface (110) [25,26]. On this surface all oxygen atoms in the terminal layer indicated in Fig. 5 are 2nd NN to oxygen atoms on the (110) plane and 1st NN to atoms lying on the subsurface layer (site A in Fig. 5). We have calculated the DOS for both the stoichiometric (110) surface and for this surface with an oxygen vacancy 1st NN. In Fig. 8 we show the oxygen DOS of the stoichiometric SnO_2 and stoichiometric and defective (110) surfaces. Changes in the band gap are clearly observable. The stoichiometric surface shows a reduction in the band gap. For the nonstoichiometric surface a dispersed band arises in the band gap showing a significant density of states that reduces it to about 0.5 eV. These results are in agreement with previous experimental results and ground-state calculations [31,45]. The effect of such a broad intragap band on the EELS spectrum is to produce a broad prepeak at the same energy of those in Fig. 7 with a long tail to lower energies (not shown).

V. CONCLUSIONS

In this paper, we have investigated the effects of oxygen vacancies on the EELS and electronic structure of SnO_2 using calculations based on real-space multiple scattering as well as LAPW. Comparison to high quality experimental EELS data of stoichiometric SnO_2 shows that quantitative agreement can be achieved when fully nonspherical potentials are used and quasiparticle and vibrational effects are accounted for. We also have investigated the effects of single oxygen vacancies on the DOS and EELS spectra of SnO_2 and evaluated the impact of vacancies on the (110) surface. Our results show the sensitivity of the EELS and unoccupied states to oxygen defects, producing a preedge peak related to the unoccupied defect state. Due to this sensitivity, high quality theoretical modeling combined with the high spatial and energy resolutions of EELS experiments makes EELS a powerful tool for characterizing defects in SnO_2.

[1] P. Dai, L. Zhang, G. Li, Z. Sun, X. Liu, and M. Wu, Mater. Res. Bull. **50**, 440 (2014).

[2] W. Zeng, H. Zhang, Y. Li, W. Chen, and Z. Wang, Mater. Res. Bull. **57**, 91 (2014).

[3] Z. R. Dai, Z. W. Pan, and Z. L. Wang, Adv. Funct. Mater. **13**, 9 (2003).

[4] Y. Shimizu, in *Encyclopedia of Applied Electrochemistry*, edited by G. Kreysa *et al.* (Springer, New York, 2014), pp.1974–1982.

[5] T. Kim, D. Lee, and Y. Yoon, J. Appl. Phys. **88**, 3759 (2000).

[6] R. Asahi, T. Morikawa, T. Ohwaki, K. Aoki, and Y. Taga, Science **293**, 269 (2001).

[7] A. Kowal, M. Li, M. Shao, K. Sasaki, M. B. Vukmirovic, J. Zhang, N. S. Marinkovic, P. Liu, A. I. Frenkel, and R. R. Adzic, Nat. Mater. **8**, 325 (2009).

[8] M. S. Arnold, P. Avouris, Z. W. Pan, and Z. L. Wang, J. Phys. Chem. B **107**, 659 (2002).

[9] H.-C. Wu *et al.*, Adv. Funct. Mater. **21**, 474 (2011).

[10] S. Trost *et al.*, Adv. Energy Mater. **6**, 1600347 (2016).

[11] Z. Dong *et al.*, Adv. Mater. **26**, 905 (2014).

[12] R. Tian *et al.*, Sci. Rep. **6**, 19195 (2016).

[13] N. Wan *et al.*, Sci. Rep. **6**, 18978 (2016).

[14] D. Zhou, W. Song, X. Li, and L.-Z. Fan, ACS Appl. Mater. Interfaces. **8**, 13410 (2016).

[15] Y. Liu, Y. Jiao, Z. Zhang, F. Qu, A. Umar, and X. Wu, ACS Appl. Mater. Interfaces **6**, 2174 (2014).

[16] D. V. Shinde *et al.*, RSC Adv. **3**, 9431 (2013).

[17] V. R. Shinde, T. P. Gujar, and C. D. Lokhande, Sens. Actuators, B **123**, 701 (2007).

[18] Y. V. Kaneti, Z. Zhang, J. Yue, Q. M. D. Zakaria, C. Chen, and X. Jiang *et al.*, Phys. Chem. Chem. Phys. **16**, 11471 (2014).

[19] A. Chowdhuri, S. K. Singh, K. Sreenivas, and V. Gupta, Sens. Actuators, B **145**, 155 (2010).

[20] Z. Lin, N. Li, Z. Chen, and P. Fu, Sens. Actuators, B **239**, 501 (2017).

[21] Y. Wang *et al.*, Sens. Actuators, B **240**, 1321 (2017).

[22] H. Wang, K. Dou, W. Y. Teoh, Y. Zhan, T. F. Hung, F. Zhang, J. Xu, R. Zhang, and A. L. Rogach, Adv. Funct. Mater. **23**, 4847 (2013).

[23] J. D. Prades *et al.*, Sens. Actuators, B **126**, 6 (2007).

[24] V. Kumar, V. Kumar, S. Som, J. H. Neethling, E. Olivier, O. M. Ntwaeaborwa, and H. C. Swart, Nanotechnology **25**, 135701 (2014).

[25] M. Epifani *et al.*, J. Phys. Chem. C **112**, 19540 (2008).

[26] V. Bonu, A. Das, A. K. Prasad, N. G. Krishna, S. Dhara, and A. K. Tyagi, Appl. Phys. Lett. **105**, 243102 (2014).

[27] J. Mizusaki, H. Koinuma, J.-I. Shimoyama, M. Kawasaki, and K. Fueki, J. Solid State Chem. **88**, 443 (1990).

[28] S. Samson and C. G. Fonstad, J. Appl. Phys. **44**, 4618 (1973).

[29] P. Ágoston, K. Albe, R. M. Nieminen, and M. J. Puska, Phys. Rev. Lett. **103**, 245501 (2009).

[30] K. G. Godinho, A. Walsh, and G. W. Watson, J. Phys. Chem. C **113**, 439 (2009).

[31] F. Trani, M.Causà, D. Ninno, G. Cantele, and V. Barone, Phys. Rev. B **77**, 245410 (2008).

[32] J. Haeberle *et al.*, J. Appl. Phys. **120**, 105101 (2016).

[33] M. A. Figueiredo and J. Mirão, Eur. J. Miner. **14**, 1061 (2002).

[34] C. McGuinness, C. B. Stagarescu, P. J. Ryan, J. E. Downes, D. Fu, K. E. Smith, and R. G. Egdell, Phys. Rev. B **68**, 165104 (2003).

[35] S. O. Kucheyev, T. F. Baumann, P. A. Sterne, Y. M. Wang, T. van Buuren, A. V. Hamza, L. J. Terminello, and T. M. Willey, Phys. Rev. B **72**, 035404 (2005).

[36] M. S. Moreno, R. F. Egerton, J. J. Rehr, and P. A. Midgley, Phys. Rev. B **71**, 035103 (2005).

[37] R. F. Egerton, *Electron Energy-Loss Spectroscopy in the Electron Microscope*, 3rd ed. (Springer, New York, 2011).

[38] J. J. Kas, A. P. Sorini, M. P. Prange, L. W. Cambell, J. A. Soininen, and J. J. Rehr, Phys. Rev. B. **76**, 195116 (2007).

[39] F. Fossard, G. Hug, K. Gilmore, J. J. Kas, J. J. Rehr, F. D. Vila, and E. L. Shirley, Phys. Rev. B **95**, 115112 (2017).

[40] P. Blaha, K. Schwarz, G. Madsen, D. Kvasnicka, and J. Luitz, WIEN2K, An Augmented Plane Wave + Local Orbital Program for Calculating Crystal Properties. Karlheinz Schwarz, Technical University, Wien, Austria.

[41] K. Jorissen, The *ab initio* calculation of relativistic electron energy loss spectra, Ph.D. thesis, University of Antwerp, 2007.

[42] A. A. Bolzan, C. Fong, B. J. Kennedy, and C. J. Howard, Acta Crystallogr., Sect. B: Struct. Sci. **53**, 373 (1997).

[43] J. P. Perdew, K. Burke, and M. Ernzerhof, Phys. Rev. Lett. **77**, 3865 (1996).

[44] S. I. Kurganskii *et al.*, Phys. Solid State **56**, 1748 (2014).

[45] J. J. Rehr *et al.*, Phys. Chem. Chem. Phys. **12**, 5503 (2010).

[46] J. J. Rehr and R. C. Albers, Rev. Mod. Phys. **72**, 621 (2000).

[47] A. L. Ankudinov, B. Ravel, J. J. Rehr, and S. D. Conradson, Phys. Rev. B **58**, 7565 (1998).

[48] M. S. Moreno, K. Jorissen, and J. J. Rehr, Micron **38**, 1 (2007).

[49] P. D. Borges, L. M. R. Scolfaro, H. W. Leite Alves, and E. F. da Silva, Jr., Theor. Chem. Acc. **126**, 39 (2010).

[50] D. Grandjean, R. E. Benfield, C. Nayral, A. Maisonnat, and B. Chaudret, J. Phys. Chem. B **108**, 8876 (2004).

[51] J. J. Kas, J. Vinson, N. Trcera, D. Cabaret, E. L. Shirley, and J. J. Rehr, J. Phys.: Conf. Ser. **190**, 012009 (2009).

[52] D. F. Cox, T. B. Fryberger, and S. Semancik, Phys. Rev. B **38**, 2072 (1988).